Nanoscale

ROYAL SOCIETY OF CHEMISTRY

PAPER

View Article Online
View Journal

Check for updates

Cite this: DOI: 10.1039/d5nr04865f

Vacancy-driven twinning in metal nanoparticles: from bulk morphology transformation to optical and electrochemical effects

Ilia Smirnov, *[a] Zbigniew Kaszkur, *[b] Mohit Chaudhary, [c,d] Hans-Christian Weissker, [c,d] Riccardo Ferrando [e] and Pawel J. Kulesza [a]

Received 17th November 2025,
Accepted 31st December 2025

DOI: 10.1039/d5nr04865f

rsc.li/nanoscale

Stacking defects in noble metal nanoparticles influence their optical, catalytic, and electrical properties, but the mechanisms behind these changes are in many cases not well understood. While some mechanisms behind the formation of stacking defects have been studied, the possibility to deliberately manipulate the nanoparticle bulk morphology remains largely unexplored. Here, we introduce a vacancy-driven twinning mechanism that transforms face-centered cubic (fcc) gold nanoparticles into locally hexagonal close-packed (hcp) structures upon reaching a critical vacancy concentration. Atomistic simulations reveal that this transformation leads to multiply twinned morphologies, including cross-twinning patterns and stable hcp domains spanning 2–6 atomic layers. Experimentally, we validate this mechanism through thermal treatment of Au–Pt alloy nanoparticles, with multidomain X-ray diffraction (MDXRD) confirming controllable ordering and disordering transitions in the bulk structure. Furthermore, we investigate how the nanoparticles' bulk morphology influences their optical properties. Using time-dependent density-functional theory with Hubbard *U* corrections (TDDFT+*U*), we analyze the plasmonic response of models with specific defect motifs demonstrating that structural defects influence the absorption profile. Finally, we discuss how these morphology-induced changes in the electronic structure and plasmonic behavior could potentially modulate electrochemical activity in catalytic systems.

Introduction

Face-centered cubic (fcc) metal nanoparticles (NPs) have attracted significant attention due to their unique physical and chemical properties. Most studies focus on size, shape, and size distribution as the primary factors determining nanoparticle behavior. However, bulk defect structures, such as stacking faults and twinning, are often overlooked, despite their potential influence on the optical, electronic[1–4] and catalytical[5–9] properties of NPs.

Commonly studied fcc nanocrystals include cuboctahedra (CUB), decahedra (DEC), and icosahedra (ICO). DEC and ICO structures arise from coalescence[10,11] or stepwise/random nucleation[12–14] of fcc segments, forming ordered twin boundaries. However, these formation mechanisms do not fully capture the diversity of possible nanostructures or allow for controlled manipulation of the morphology.

Existing studies on morphology control primarily focus on the transition from the fcc phase to hexagonal close-packed (hcp) structures in metals such as Au,[15–19] Rh,[20] Ag,[1,21] Ni[22,23] *etc*. Most of these particles are non-equilibrium-shaped particles with a bulk morphology that differs from the lowest energy minimum state. Despite advances in experimental synthesis and computational modeling, a comprehensive understanding of how defects form, stabilize, and affect the material's properties remains elusive.

In the chemical literature, diffraction patterns of fcc metals frequently display multitwinning characteristics. As predicted by Warren, the 111 and 200 peaks converge, forming 'bridge' intensities as the crystal size decreases.[24] The intensity ratio of 200, 220 to 111 often exceeds values estimated for perfect crystals. Multitwinning in fcc metal nanocrystals synthesized *via* chemical routes appears to be a common feature. Contrarily, computer simulations often suggest that condensing metal vapors tend to order easily, leaving little room for defects. However, these vapors can create faulty stacking on faces leading to defects.[12] As (111) faces grow slowly, local seeds quickly form octahedral shapes. Further growth is accelerated by local twinning and condensation in grooves, as proposed by

---

[a] *Faculty of Chemistry, University of Warsaw, ul. Pasteura 1, Warsaw, 02-093, Poland. E-mail: snowwhiteman42@gmail.com, i.smirnov@uw.edu.pl*
[b] *Institute of Physical Chemistry, Polish Academy of Sciences, Kasprzaka 44/52, Warsaw, 01-224, Poland. E-mail: zkaszkur@ichf.edu.pl*
[c] *Aix Marseille Univ., CNRS, CINaM, Marseille, France*
[d] *European Theoretical Spectroscopy Facility, https://www.etsf.eu*
[e] *Dipartimento di Fisica, Università di Genova, Via Dodecaneso 33, 16146 Genova, Italy*

the Witten–Helffer–Sjostrand theory and extended by van de Waal.[25–27] Low-temperature chemical reduction can cause significant local disorder with possible vacancies, rapidly relaxing to multitwinned forms. The vacancy-driven construction of realistic multitwinned models offers greater flexibility and reduced computational costs.

Since stacking defects alter the local electronic structure, their presence is expected to impact the optical properties of nanoparticles.[28,29] Recent studies[30–32] indicate that twinning influences both Raman and plasmonic properties by altering the vibrational density of states and modifying the local dielectric environment. Raman scattering experiments show that well-ordered single-crystal nanoparticles exhibit intense quadrupolar modes, whereas their multiply twinned counterparts lack this feature. Similarly, plasmonic studies demonstrate[33] that twinning leads to localized surface plasmon resonance (LSPR) damping and an enhanced scattering process.[34] However, such studies provided only phenomenological description partially based on the Mie theory. A more accurate understanding requires explicitly accounting for quantum effects while isolating the influence of morphology from other factors such as size and shape.

To investigate the impact of stacking defects on plasmonic behavior, we designed two sets of models, each containing one defect-free fcc nanoparticle and another incorporating structural defects (stacking faults or twin planes). By ensuring that both defective and single-domain models maintained a nearly identical outer shape and size, we isolated the effect of stacking defects on plasmonic response as far as possible. Using the recently developed time-dependent density functional theory with Hubbard *U* corrections[35] (TDDFT+*U*) which has been shown to perform very well for silver clusters[36] but also for gold clusters,[37] we demonstrated that twinning alters the electronic structure as illustrated by the superatomic projected density of states, and it leads to changes in the height and width of the plasmon absorption pattern.

Furthermore, we introduce a vacancy-driven twinning (VDT) mechanism as a theoretical framework to explain stacking defect formation (Fig. 1). To validate our model, we performed molecular dynamics (MD) simulations on CUB Au nanoparticles populated with vacancies, using the Sutton–Chen (SC) and Gupta potentials for medium-scale modeling of metal nanoparticles. The results revealed locally ordered (2–6 layers thick) hcp domains, 2D and 3D cross-twinning patterns, and structural features not previously reported in computational studies.

To experimentally verify the proposed concepts, we applied X-ray diffraction (XRD) and small-angle X-ray scattering (SAXS) techniques to quantify the bulk morphology in AuPt nanoparticle samples. The degree of twinning (*i.e.*, the number of domains) was estimated using a multidomain XRD approach (MDXRD),[38] while the nanoparticle density and size were analyzed through SAXS diffraction patterns calculated *via* the Debye formula. These methods provide a simple alternative to three-dimensional transmission electron microscopy for routine analysis of the bulk morphology.

Our work aims to bridge the gap between atomic-scale defect formation, plasmonic behavior, and crystalline engineering techniques. By elucidating the role of stacking defects in the nanoparticle morphology and optical response, we provide insights into the fundamental mechanisms governing fcc metal nanostructures' morphology and propose new strategies for their controlled synthesis and application.

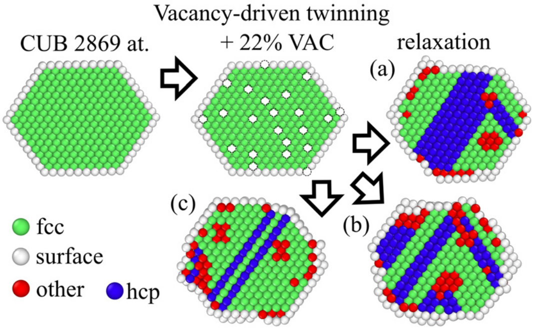

Fig. 1 Schematic representation of vacancy-driven twinning. Starting from a strain-free raw model of CUB with 2869 atoms, 22% of the atoms were randomly removed. Depending on the initial vacancy distribution, the relaxation resulted in varying structural configurations (a, b, c models). The cross-sections of the analyzed clusters show four types of atoms: fcc, hcp, other, and surface atoms. Crystal structure analysis was performed using OVITO software.[39]

Results and discussion

Effect of vacancies on nanoparticle bulk morphology: simulation results

To populate fcc NPs with vacancies, we randomly delete atoms from initially strain-free models. Then, the obtained models are relaxed or heated up with MD simulation using the Sutton–Chen or Gupta potential. Energy minimization leads to highly disordered structures with partially preserved vacancies. Upon MD heating, vacancies in disordered clusters tend to diffuse toward the surface, resulting in partial ordering of the internal structure.

To study the disordering of fcc stacking, we populated raw CUBs of various sizes (11 models) with 0 to 22% of vacancies and relaxed them using the SC potential (Table 1, Cluster software[40,41]). To characterize the degree of twinning, we calculated the XRD patterns of the corresponding models and analyzed the number of domains (Num.dom.) with the multidomain XRD (MDXRD) approach.[38] Short comments on the physical meaning of Num.dom., MDXRD and other bulk analysis methods can be found in Note S1 and Fig. S1.

We noticed that there are several factors affecting vacancy-driven twinning: first of all, a size dependency of VDT. The smaller a cluster, the higher the percentage of atoms on a surface. Therefore, while creating vacancies in small NPs (by random removal of atoms), there will be an increased number of surface voids that do not lead to bulk twinning. Another critical aspect is an effective conversion of vacancies to stacking faults. One can imagine that there are spatial arrangements of vacancies (their combination/sequences) that will

Table 1 Number of domains in relaxed gold CUBs saturated with different percentages of vacancies

	Vacancies [%]; relaxed models								
CUB, atoms	0	8	10	12	14	16	18	20	22
923	1.1	1.3	1.1	1.2	3.5	2.9	8.3	6.1	7.5
1415	1.1	1.3	1.3	1.1	4.3	3.4	3.8	7.3	6.6
2057	1.1	1.1	1.1	1.2	1.2	1.5	4.0	3.7	5.3
2869	1.0	1.1	1.1	1.2	1.2	1.6	5.6	8.8	**3.8**^{1}
3871	1.1	1.1	1.0	1.1	1.5	4.6	2.6	4.4	**7.7**^{2}
5083	1.0	1.1	1.1	1.1	1.9	2.9	4.3	8.8	7.8
6525	1.0	1.1	1.1	1.1	1.1	6.1	10.3	5.5	8.0
10 179	1.0	1.1	1.1	1.2	1.2	6.0	7.7	12.6	5.1
14 993	1.0	1.1	1.2	1.3	1.3	10.1	**6.5**^{3}	**8.9**^{4}	13.0
21 127	1.0	1.1	1.1	1.2	2.2	6.2	8.0	13.0	
28 741	1.0	1.2	1.2	1.3	1.3	8.4	10.1	13.0	

Number of domains
1
3
5
7
9
11
13
15

Corresponding calculated XRD patterns of multidomain particles were analyzed using the MDXRD method. This method provided information on the degree of twinning, which is shown as the number of domains: from 1 domain (green) to 13 domains (red). More details in Note S2. Models superscripted with numbers 1–4 will be discussed in the following section.

affect the initial structure stronger than others. All these features are less influential in large NPs where most vacancies will likely be created in the bulk, and their distribution can be considered uniform.

To minimize the randomness in vacancy distribution, we considered averaging the results in Table 1 over different-size CUBs. It allowed us to determine the average critical concentration of vacancies necessary to cause twinning in CUB models (Fig. 2). In the case of randomly distributed vacancies, it equals ~13.1%. However, there might be spatial arrangements of vacancies that can cause twinning at even lower concentrations.

Formation of hcp layers and stacking patterns

Among the simulated models in Table 1, there are some in which XRD patterns have an additional diffraction peak between 111 and 200 peaks, corresponding to the 101 peaks of the hcp Au phase. Fig. 3 shows these hcp-containing clusters superscripted by numbers 1–4 in Table 1. It seems that the intensity of the hcp phase peak is dependent not only on the total amount of hcp-phase atoms, but also on their distribution and forming multilayer structures. Even though models 3 and 4 (Fig. 3) have similar fractions of hcp arranged atoms, only model 3 has a noticeable additional diffraction peak.

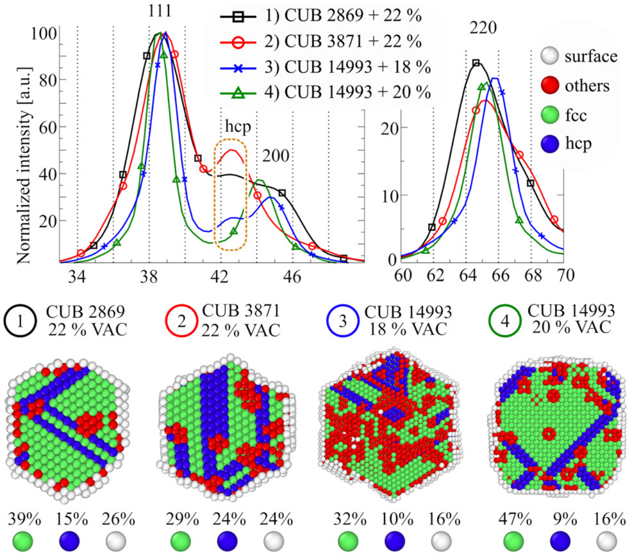

Fig. 3 Calculated XRD patterns of multidomain models with hcp layers. The cross-section of the analyzed clusters shows four types of atoms: fcc, hcp, other, and surface (OVITO software).

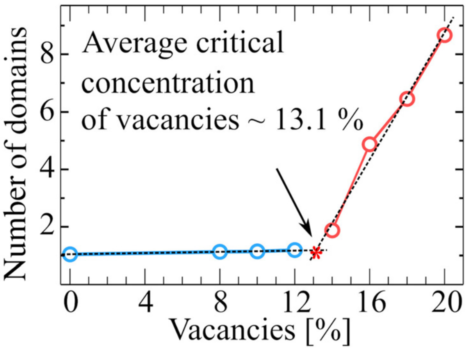

Fig. 2 The dependence of the number of domains on the amount of vacancies. Blue points correspond to models with nearly one domain, and pink points represent multiply twinned particles. The intersection of these lines corresponds to the lowest concentration of vacancies at which twinning is likely.

Among all simulated models, the most interesting is CUB 2869 + 22% (Fig. 3, model 2, a red line with circles). Its crystal structure analysis revealed a 4-layer thick hcp (2H type) domain. By adding two more percent of vacancies (24% in total), the energy minimization led to the appearance of a locally six-layer thick hcp (2H type) segment. To our knowledge, computational simulations have not previously described the local hcp phase formation from an fcc framework *via* relaxation.

However, the obtained 4- and 6-layer thick hcp fragments were not stable upon heating at 293 K. These hcp fragments tend to break up into single hcp layers or two 2-layer hcp segments separated by fcc layers (Fig. S2). Most likely, it's because these fragments don't penetrate the whole cluster, making them unstable during heating. This observation highlights the importance of a first step in obtaining randomly twinned NPs. Energy minimization of models with vacancies allows for the simulation of defect-rich but unstable models. Meanwhile, the molecular dynamics produces more stable and ordered structures.

Besides the appearance of the hcp phase, we found a characteristic cross-twinning pattern that was not described in the literature (Fig. 4). This pattern consists of four stacking faults originating from a common center, resulting in a 2 dimensional "X"-like pattern. Although this pattern frequently appeared in the models listed in Table 1, none were stable or well-formed. Therefore, a 4-domain model was constructed manually (Method S1). An ideal one domain CUB (2057 atoms) was cut into four pieces; then their positions were adjusted to create four hcp-like stacking planes between domains.

The stability of nanoparticles depends on their potential energy per atom, which is influenced by the surface configuration. The 4-domain model, derived from the ideal CUB, has nearly identical surface planes to the mother structure. Despite subtle contributions from stacking and surface defects, the 4-domain cluster is as stable as the original 1-domain CUB (Note S3). MD simulations confirm the stability of the 4-domain structure up to the melting temperature.

Fig. 4 illustrates the two-dimensional cross-twinning pattern, which is not the only possible pattern. The detailed analysis of models described in Table 1 revealed three-dimensional ones. This cross-twinning has an “X”-like pattern (similar to Fig. 4) and lies in three dimensions. In fact, stacking faults coincide with imaginary planes between CUB edges and a central point (24 planes). Similar to the previous case, energy minimization of software-generated models did produce a well-ordered cross-twinning pattern. It only indicated such a possibility. We tried to build this model manually, but the final 14-domain structure is unstable and tends to collapse during relaxation (Data S2).

Thermal evolution of multidomain nanoparticles

The relaxed multidomain particles have multiple bulk and surface defects leading to high potential energy in a system (Fig. S3). Applying external energy can increase the atom mobility, leading to defect diffusion followed by surface and bulk rearrangement. We heated multidomain NPs using MD simulations and analyzed their changes using X-ray diffraction in a wide and small-angle X-ray scattering range.

Since the SAXS technique is sensitive to the shape of particles, we used an ideal fcc ball with 5089 atoms as an initial structure. Then the ball was populated with 0–22% of vacancies, relaxed, and slowly heated to the melting temperature. All the results can be seen in Tables S1–S4.

Fig. 5 demonstrates some features of the structural evolution of the ball model with 22% of vacancies, where the top part of the picture (Fig. 5(a)) provides a visual illustration of the evolution. After initial relaxation, the cluster structure became significantly distorted, with a substantial number of vacancies preserved (represented by red balls: atoms neighboring vacancies). Consequently, this structure exhibits high

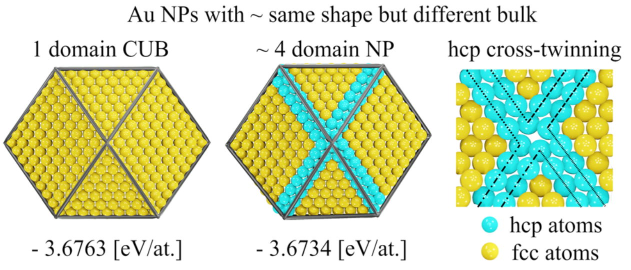

Fig. 4 1-domain CUB (2057 atoms) and manually created 4-domain cluster. All models were relaxed with the SC potential. Values below the models correspond to potential energies per atom.

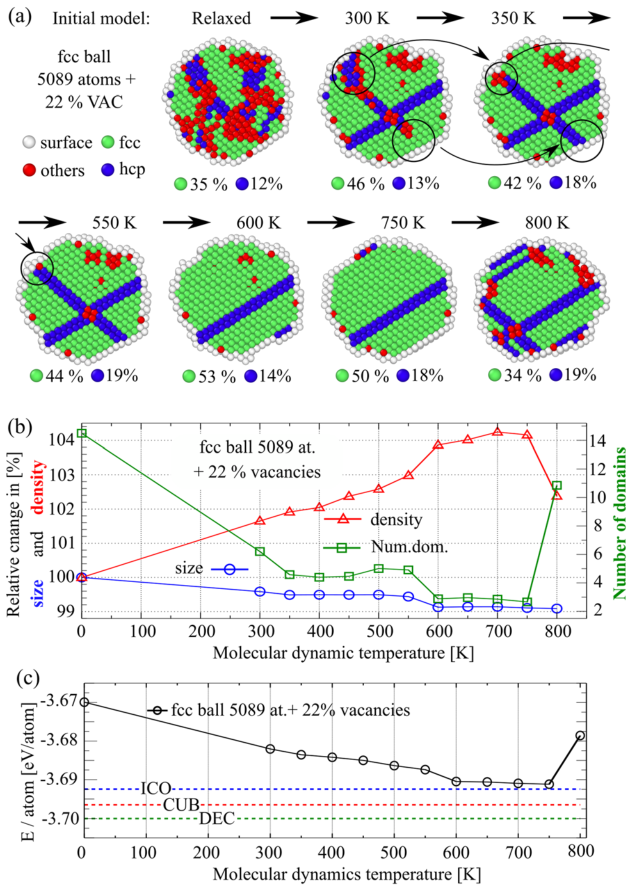

Fig. 5 (a) Evolution of the multidomain NP structure with temperature. Cross-sections of fcc ball models with 22% vacancies after relaxation and subsequent MD simulations (SC potential). The duration of each MD period was no less than 50 psec, and after each heating, the clusters were relaxed. (b) The left *Y*-axis shows relative changes in density (red triangles) and mean size (black circles) calculated *via* SAXS. The right *Y*-axis represents the number of domains (green squares) determined by MDXRD. (c) The graph illustrates changes in potential energy per atom after the heating. Blue, red, and green dotted lines correspond to ICO, CUB, and DEC structures of the same size (Data S1).

potential energy (Fig. 5(c)), and only "precursor" areas for future twin planes have been formed. Following MD simulation at 300 K, these regions undergo ordering: two new stacking faults formed, and plane faults ordering is in progress. As the temperature increases from 300 K to 550 K, the vacancies diffuse toward the surface (Fig. 5(a); depicted by a sequence of black circles with arrows).

As the vacancy concentration decreases, the overall density tends to increase. To validate this assumption for each multidomain model, we analyzed the corresponding SAXS patterns within the q range of 0.01–0.5 Å^{-1}. Fig. 5(b) illustrates how high-temperature treatment increases the density and reduces the mean size. However, upon reaching the premelting temperature (800 K), the cluster accumulates vacancies again, causing secondary twinning. This observation aligns qualitatively with multiple experimental findings[42,43] showing that the concentration of vacancies increases when approaching the melting point.

Fig. 5(c) depicts the change in the potential energy per atom as a function of MD temperature. Remarkably, across the entire temperature range (0–800 K), the density change (Fig. 5(b)) correlates proportionally to the potential energy change (Fig. 5(c)). Interestingly, the slight increase in the number of domains after 500 K did not affect this trend. We noticed that vacancies contribute more significantly to the increase in potential energy than twin planes. When the void concentration is low, multidomain structure stability is comparable to regular ICO, DEC, and CUB morphologies.

A comparison of a one-domain CUB and 4-domain structures (Fig. 4 and Note S3), shows that surface is the most important modifier of the total energy (if there are no vacancies inside). The potential energy per atom analysis neglects the bulk morphology because the most significant energy changes come from not fully coordinated atoms, *i.e.* from those neighboring voids and from the surface. However, it might be a critical threshold in the understanding of formation and growth of NPs. To our knowledge, despite their stability comparable to CUB structures, 4-domain structures have not been observed experimentally. It is likely because of the internal strains created by hcp cross-stacking.

Influence of interatomic potentials on VDT behavior: Sutton–Chen *vs.* Gupta

Also, we tested the dependency of VDT on the interatomic potentials. The previously obtained results (using SC potential) were compared with simulations based on the Gupta potential. Despite some quantitative differences, all trends remain the same. The CUB (2869 atoms) saturated with 8% of vacancies showed no twinning and was stable. In the case of 22% of vacancies, the raw CUB structure transformed into a multiply twinned one. The number of domains was similar in both models: relaxed with the SC and Gupta potentials (Fig. S4).

To test how the interatomic potential affects the temperature-induced ordering, we repeated the simulation from Fig. 5. We started from the same prerelaxed model (fcc ball 5089 at + 22% of vacancies) using the Gupta potential. Again, despite some quantitative differences, all trends are confirmed. The higher the temperature, the more ordered the structure (Fig. S5). Close to the melting temperature, some vacancies penetrated the bulk and caused secondary twinning. The melting temperature obtained by SC and Gupta potentials is slightly different, ~800 and 850 K, respectively, so that in the Gupta potential the same phenomena tend to appear at a slightly higher temperature.

In summary, both potentials provide qualitatively similar results. However, it is difficult to compare exactly SC and Gupta's potentials in VDT studies as both approaches explore energy relaxation in different ways. During energy minimization the models with vacancies suffer a series of quick reconfigurations intertwined with periods of slow relaxation (Fig. S6). In the complex energy landscape, different potentials and algorithms (conjugated gradients, Hessian, *etc.*) can follow slightly different paths arriving at different local minima, which however present the same type of vacancy arrangement.

Influence of vacancy distribution on morphology evolution

As shown in Table 1, even when the vacancy concentration is high, strong twinning does not necessarily occur. For instance, CUBs composed of 10 179 atoms with 20% and 22% vacancy concentrations results in structures with 12.6 and 5.1 domains, respectively. This indicates that VDT is highly sensitive to the initial positions (distribution) of vacancies within the bulk.

To investigate the effect of vacancy distribution, we conducted a series of relaxation simulations (SC potential) on the raw CUB 2869 structure with 22% of defects. In each simulation, the positions of the vacancies were randomly assigned. A total of twelve independent simulations were performed, and the resulting XRD patterns were analyzed to assess the variations in bulk morphology.

The resulting models exhibited significant differences (Fig. S7). Fig. 6 demonstrates the substantial impact that the

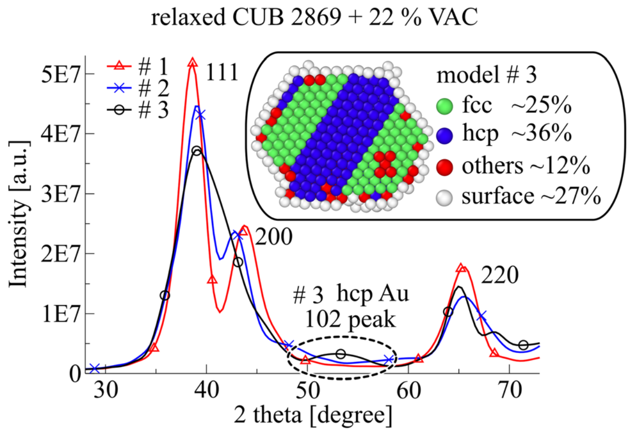

Fig. 6 Probing different spatial arrangements of vacancies. The given models illustrate the weakly (red line), moderate (blue line), and strongly (black line) defective structures. The cross-section of the multidomain NP with a 6-layer thick hcp phase corresponds to model #3.

initial positions of voids (with a constant vacancy concentration) can have on the final structure. The red XRD pattern (model #1) displays distinct, well-separated, and narrow diffraction peaks, indicating weak twinning. In contrast, the blue XRD pattern (model #2) shows a noticeable overlap of the 111 and 200 peaks and a broadened 220 peak, suggesting moderate twinning. The black XRD pattern (model #3) features a pronounced overlap of the 111 and 200 peaks, along with a complex profile for the 220 peak, which suggests that this model is heavily defective.

Among the analyzed models, model #3 provides an XRD pattern with an extra XRD peak at ~53.2 degrees that has not been seen for other models. This weak peak corresponds to the hcp gold phase and appeared because of the 6-layer thick hexagonal phase. Unlike the previously discussed 4–6 thick hcp layers (*i.e.* Fig. 3, model #2), this one penetrates the whole cluster and looks similar to the experimentally observed fcc-2H-fcc gold nanorods 16. MD simulations (SC potential) showed that model #3 is stable up to the melting temperature. During MD heating, all previously described trends remain valid: as the temperature rises, the preserved vacancies diffuse to the surface; the stacking layers heal defects and become more ordered.

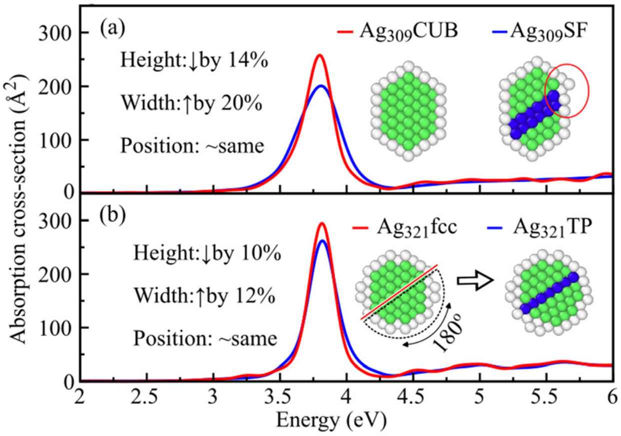

Fig. 7 Calculated absorption spectra of (a) regular silver CUB (Ag_{309} CUB, red line) and CUB-derivative with a stacking fault (Ag_{309} SF, blue line), both consisting of 309 atoms; (b) ideal fcc silver sphere (Ag_{321} fcc, red line) and sphere-derivative with a twin plane (Ag_{321} TP, blue line), both consisting of 321 atoms. The cluster models shown are cross-sections through the middle of clusters; white, green and blue spheres represent surface, fcc and hcp atoms, respectively (determined by OVITO software). All models were relaxed using VASP,[44,45] utilizing PBE to approximate the exchange–correlation functional, until the forces on each atom were reduced to less than 0.01 eV Å^{-1}.

Impact of stacking defects on plasmonic response

It is well known that plasmonic properties depend on the distribution of the electron density, making them highly sensitive to size, shape, composition, and the surrounding dielectric environment. To isolate the effect of bulk morphology alone, all other factors, particularly shape, must be controlled.

To address this, we manually constructed (Method S1) two sets of models with nearly identical shapes but different internal structures. Since the CUB shape is one of the most commonly accepted structures for nanoclusters, we first compared a regular silver CUB (Ag_{309} CUB) with a CUB-like model containing a single stacking fault at its center (Ag_{309} SF). Fig. 7(a) illustrates the absorption cross-section against energy, obtained using real-time time-dependent density functional theory (RT-TDDFT+U) with an effective-U Hubbard correction of 4 eV.[36,37]

Clearly, the introduction of a stacking fault broadens the plasmonic response of the clusters. While Ag_{309} SF retains a cuboctahedron-like shape, its stacking fault introduces a shift in packing layers, creating additional edge defects adjacent to the regular fcc domains (*e.g.*, the most prominent defect is highlighted in Fig. 7(a) with a red circle). However, one cannot easily estimate the impact of the overall shape change on the absorption response. The change of the spectra following the introduction of both the stacking fault and the minor shape alteration suggests that morphology-dependent plasmonic effects cannot be fully disentangled from shape-induced effects in these models, as is clear from the direction-resolved absorption curves shown in supplementary Fig. S8.

To eliminate shape-related influences as much as possible, we constructed a second set of models (Fig. 7(b)): a nearly spherical fcc-based cluster (Ag_{321} fcc) and a structurally almost identical counterpart containing a twin plane (Ag_{321} TP). The model with the defect was generated directly from the fcc sphere by rotating half of the atoms by 180° (Method S1), ensuring nearly identical energies per atom, surface structures, and overall shapes (Fig. S9). These models enable a more direct assessment of how stacking defects affect plasmonic behavior while minimizing shape-related artifacts. The absorption curves for the identical fcc-spheres, shown in Fig. 7(b), follow the same trend as the Ag_{309} cubeoctahedron-like clusters, except that the broadening in the latter is significantly reduced. In neither case, significant shifts in LSPR energies are observed.[36]

The broadening of the LSPR peak following the introduction of a stacking fault can be directly linked to modifications in the electronic ground state, particularly the delocalized 5s electrons near the HOMO. While atomic 4d electrons play a crucial role in dynamically screening the coherent oscillation of the 5s electrons in the LSPR, they are less significant in our analysis, given that we are comparing clusters of similar size and shape while keeping the value of the effective Hubbard U fixed to 4 eV. The atomic 5s electrons in such systems are known to arrange themselves into 'superatom' states, forming discrete quantum states similar to atomic orbitals S, P, D, and so on.

In Fig. 8(a) and (b), we present the superatomic projected density of states (SAC PDOS) for fcc spheres, both with and without the stacking fault. The SAC PDOS was calculated by projecting individual Kohn–Sham wavefunctions onto spherical harmonics of specific angular momentum character, centered at the clusters' center of mass. The system contains 321 delocalized atomic s electrons, which is a relatively large

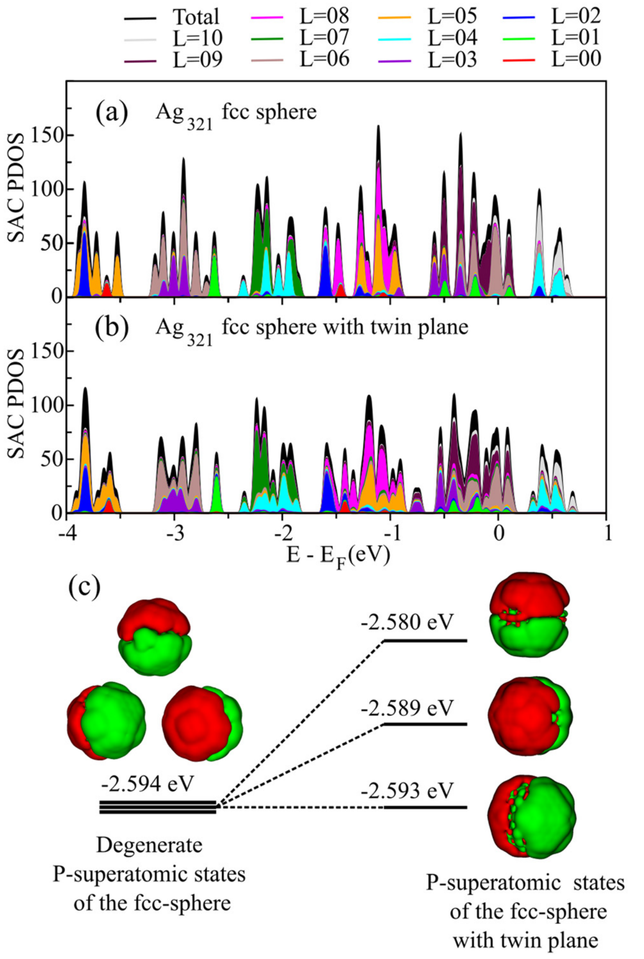

Fig. 8 Calculated superatomic projected density of states for (a) a regular Ag_{321} fcc-sphere and (b) an fcc-sphere with a twin-plane stacking fault. The HOMO in both plots is shifted to 0 eV. For clarity, the contributions of the 4d states, which start at −4 eV below the HOMO, are not shown. (c) Visualization of the wavefunction for the three degenerate P-superatomic states in the defect-free fcc sphere (left) and the modified states after introducing the twin-plane defect, leading to the lifting of the degeneracy.

number. Therefore, we performed the projection up to $L = 10$. In our representation of SAC PDOS, we display contributions from different L values stacked on top of each other, showing how well the sum of our projections compares to the total density of states (DOS), shown in black. In the HOMO, we find major contributions from the states having character $L \leq 9$, while in the LUMO, $L = 10$ character starts appearing, confirming that projections up to $L = 10$ are needed in order to characterize the superatom Ag_{321} completely.

The SAC PDOS of the two clusters reveals that the electronic states exhibit a comparable overall character at all energies. This behavior is anticipated, as the delocalized 5s electrons weakly interact with the underlying atomic arrangement. However, in the fault-free structure, the density of states (DOS) features sharper and more well-defined peaks, indicating that the SAC states retain the influence of the cluster's inherent symmetry.[46]

Unlike SAC projections applied to the spherical Jellium model—where the atomic arrangement is replaced by a perfectly spherical distribution with a uniform positive background charge, yielding fully degenerate superatomic states—our DFT calculations account for deviations from the spherical shape, thereby lifting such degeneracies. A notable example is depicted in Fig. 8(c) where the P states at about 2.6 eV undergo a clear splitting upon the introduction of the twinning plane in the Au_{321} cluster. In other words, the degeneracy is lifted due to the lowering of the overall symmetry. However, this effect remains so small, due to the overall nearly spherical shape, that it is not discernible on the scale of the present SAC PDOS plots for both clusters.

A similar lifting of degeneracy can be expected for other SAC states, further contributing to the broader distribution observed in the DOS of the twinned structure. This phenomenon leads to a less pronounced peak structure compared to its fault-free counterpart, which then could translate into the broadening of the LSPR that we see clearly in our calculated absorption spectrum. Thus, we can conclude that the introduction of a stacking fault while keeping a quasi-identical shape leads to a broadening of the absorption spectra and the lifting of degeneracies in the SAC states.

Electrochemical significance

Structural defects, including stacking faults and vacancies, play a pivotal role in electrocatalysis by altering the morphology and local electronic structure of noble metal nanoparticles. These modifications affect adsorption energies and the activation of reactants or intermediates.[47] Recent studies on Au–Pt alloy systems have shown that both composition and morphology can be tuned to optimize the selectivity of various electrocatalytic reactions, for instance, promoting the selective electrochemical reduction of CO_2 to syngas ($CO + H_2$) or formic acid, enhancing O_2 reduction for fuel cell applications, and improving hydrogen evolution by increasing the electrochemically active surface area and facilitating reaction kinetics.[48]

Ongoing research is focused on optimizing not only the composition and size of Au–Pt alloy catalysts, but also their bulk crystallographic morphology to enhance the durability and catalytic performance. It has been suggested that the superior activity of such alloy electrocatalysts, relative to pure platinum, arises from lattice compression effects and modifications in the local electronic structure of Pt.[49,50] In oxidation reactions involving formic acid, methanol, and carbon monoxide, both the Au/Pt atomic ratio and the presence of stacking defects significantly affect reaction pathways and the extent of CO poisoning on Pt-rich regions.[51]

Noble metal nanostructures could also be light absorbing systems in which electron hole pairs can be formed and used as "hot" charge carriers for catalytic applications. Plasmonic effects in electrocatalysis typically refer to the use of gold or silver nanoparticles with the ultimate goal of enhancing the efficiency and selectivity of electrochemical reactions by harnessing the energy and properties of localized surface plasmon resonances. For example, by utilizing plasmonic effects, it's possible to enhance the activity and selectivity of CO_2 reduction, oxygen evolution, and hydrogen evolution.[52,53]

Taken together, these findings support the broader concept that electrocatalysts designed through defect engineering—particularly *via* controlled introduction of atomic-level imperfections—offer valuable opportunities to modulate the electronic structure, reshape the surface reactivity, increase the active site density, and improve the transport of reactants and products at the catalytic interface. The significance of stacking faults and related defects as catalytic modifiers has recently gained attention, especially in the context of efficient hydrogen generation.[54]

Vacancy-driven twinning during nanoparticle growth

The theoretical process of vacancy-driven twinning relies on a top-to-bottom approach when the removal of atoms generates vacancies. However, in reality, it is difficult (not impossible) to imagine how atoms can be extracted from the bulk of NP. Here, we propose two possible scenarios for the appearance of vacancies in real nanoparticles.

The first one is the simple atom condensation model with an intermediate step: the accumulation of vacancies (Fig. S10). During condensation, newly deposited atoms may occupy non-optimal positions away from nodal ones. As the number of such defects grows, some voids (vacancies) eventually can be formed.

Theoretical studies suggest that condensation of fcc metals in a vacuum is fast and highly effective. Even if the supply rate of condensing atoms is high, they will likely find a place corresponding to the close packing. However, in reality, in the case of the chemical synthesis route, there are always impurities, solvents, stabilizing agents, *etc*. Their presence can affect the deposition of atoms, resulting in defect formation.

Vacancy-driven twinning in bimetallic nanoparticles

Our recent experimental study suggests the appearance of the vacancy-driven twinning mechanism during the phase segregation studies of immiscible AuPt alloys.[55] Alloyed AuPt nanoparticles were heated, which triggered their growth and transformation into Janus particles. The multidomain XRD approach showed that the Pt part of the Janus particle became highly disordered and evolved with temperature, similar to the model presented in Fig. 5. Here, we report a generalized mechanism of the VDT in bimetallic fcc NPs. The detailed description can be found in our work.[42]

It is known that in bulk Au and Pt are immiscible, which is not the case at the nanoscale. Bottom-to-top approaches allow these metals to combine to form well-mixed nanoalloys. Nevertheless, once these nanoparticles grow, they possess more macroscopic-like properties and become unstable. If the temperature is high enough, it triggers the migration of gold atoms from the bulk. Therefore, gold segregates on a surface, forming Janus (or core–shell) NPs.

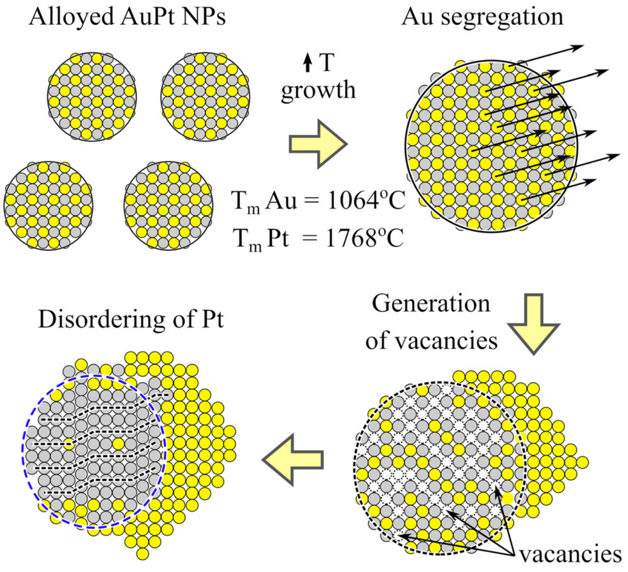

Fig. 9 Scheme of vacancy-driven twinning in bimetallic NPs during phase segregation.

While gold atoms escape the alloyed phase (Fig. 9), they leave vacancies in the bulk. Since platinum atoms are less mobile than gold, they cannot heal the generated vacancies/voids. After the concentration of generated defects exceeds a critical value, the Pt-rich phase becomes unstable and undergoes vacancy-driven twinning. As a result, the experimentally obtained Au-rich and Pt-rich phases consist of ~5 and ~20 domains, respectively. Once the system is heated further, Pt atoms become mobile enough to trigger ordering, and the number of domains decreases.

This case can be used as a guideline for initiating VDT in other fcc samples and synthesizing highly disordered monometallic NPs (Method S2). The proposed approach is similar to the Kirkendall effect, wherein during the diffusion process, atoms from the faster-diffusing metal (A) migrate into the slower-diffusing metal (B), creating vacancies within metal A. However, our method differs in two key aspects: the initial state is a homogeneous alloy (AuPt), and vacancies are generated within the metal phase of lower diffusion rate (Pt) with the higher diffusion rate atoms (Au) quickly clustering and ordering. Thus, while reminiscent of the Kirkendall effect, our approach is based on different principles.

Conclusions

In this study, we demonstrated the vacancy-driven twinning mechanism responsible for the formation of stacking defects in fcc metal nanoparticles. Above a critical vacancy concentration of ~13%, the ideal fcc stacking becomes unstable, promoting stacking faults, cross-twinning, and locally stable hcp phases. Our simulations reveal a consistent trend toward increased bulk disorder with higher vacancy concentrations and provide a computationally efficient framework for generating realistic, multitwinned nanostructures beyond conventional CUB, DEC, and ICO models.

Additionally, we explored the effect of stacking defects on the plasmonic properties using RT-TDDFT+*U* calculations, showing that such defects broaden and dampen the localized surface-plasmon resonance peak by modifying the electronic structure. Coupled with SAXS and MDXRD techniques for tracking bulk morphology evolution, the VDT approach offers a promising route for tailoring nanoparticle structures to optimize both optical and electrochemical properties. These findings provide opportunities for defect-engineered nanomaterials in photocatalysis, plasmon-enhanced reactions, and electrocatalysis, where internal morphology plays a critical role in tuning performance.

In this work, the VDT mechanism is discussed for fcc metal nanoparticles. Because it relies on metallic bonding principles, it may also apply to other simple metals (including hcp and body-centered cubic systems) and metal alloys. However, extending the concept to non-metallic nanoparticle systems would require a dedicated study, as their bonding characteristics and atomic mobility differ substantially.

Experimental

Computational simulations

Modeling of the NP structure. Raw "magic number" CUB and fcc ball models were created using Cluster.[27,38] The same software was used to populate NPs with vacancies.

We used Blender software to manually assemble NP models containing 2D and 3D hcp cross-twinn "X"-like patterns (Fig. 4 and Method S1). The initial fcc segments were created using Cluster software and then imported into Blender as a set of *XYZ* coordinates using "PDB/*XYZ*" add-on. Blender provides a convenient interface for manually editing fcc structures: moving, rotating, shaping, duplicating, *etc*. The modified structure can then be exported back as a set of *XYZ* coordinates.

Energy minimization

The energy minimization implemented in Cluster software utilizes the Sutton–Chen potential[56] and was performed until the total energy gradient reached $\sim 10 \times 10^{-6}$.

The calculations with the Gupta potential were done by using the molecular dynamics code employed in our previous studies.[12,14] Local relaxations were made by two methods, quenched molecular dynamics and quasi-Newton minimization by the Broyden–Fletcher–Goldfarb–Shanno algorithm.[57]

Molecular dynamics

The molecular dynamics algorithm implemented in Cluster software utilizes the SC potential. The simulations shown in Fig. 5 were performed as follows: a raw fcc ball consisting of 5089 atoms was populated with 22% of vacancies and relaxed. Then, the temperature was incrementally increased from 300 K to the melting point at 850 K in steps of 50 K. The duration of each stage was at least 50 ps (in thermostat mode), and the time step used was 0.001 psec. After each heating stage, the corresponding model was relaxed.

Molecular dynamics simulations (Fig. S5) were performed with the Gupta potential. We analyzed the same relaxed fcc ball made of 5089 atoms, which was populated with 22% of vacancies. The temperature incrementally increased from 300 K to 1000 K in steps of 1 K every psec. After each heating stage, the corresponding model was relaxed (using the Gupta potential) by the molecular dynamics code described in our previous studies.[12,14]

X-ray diffraction data

Powder diffraction patterns (both SAXS and wide-range scattering) were calculated using Cluster software *via* the Debye summation formula (for Cu radiation). For the analysis of XRD patterns, we used the Pearson type VII function, which is the most commonly used one. SAXS patterns were analyzed in the SASfit program,[58] assuming a spherical model with a lognormal size distribution.

Absorption spectrum

All structures were relaxed on VASP with generalized gradient approximation (GGA) as parameterized by Perdew, Burke, and Ernzerhof (PBE) to approximate the exchange and correlational functional, until forces on each atoms were less than 0.01 eV Å^{-1}.[44,45,59]

To calculate the spectra of Ag clusters, we have used the rotationally invariant formulation of DFT+*U* and subsequently RT-TDDFT+*U* as implemented in the real-space code Octopus.[35,60] For the exchange and correlation functional, we have used GGA (PBE).[59] An effective-*U* correction of 4 eV was applied to the 4d electrons of Ag atoms to account for the shortcomings of the GGA in describing localized electrons.[36] The interactions between the electrons and the ions were described using norm-conserving Troullier–Martins pseudopotentials[61] treating 11 valence electrons corresponding to 10 4d electrons and a single 5s electron in Ag explicitly. For all the calculations, the real-space grid spacing and radius were kept fixed at 0.20 Å and 5.0 Å, with the simulation box-type set to minimum. This so-called minimum refers to the radius of the sphere surrounding each atom, while the simulation box is defined as the sum of all spheres generated around each atom.

For the RT-TDDFT+*U* calculation, we have used the Yabana and Bertsch formalism,[62] which involves perturbing the electronic ground state with a δ-kick electric field at $t = 0$, followed by the time evolution of the perturbed wavefunctions. We have used the Approximated Enforced Time-Reversal Symmetry (aetrs) propagator, with a time step of ≈0.0013 fs and a total propagation time of ≈26 fs. The resulting spectrum is obtained by Fourier transforming the time-dependent dipole moment.

In both the DFT+*U* and RT-TDDFT+*U* calculations, spin–orbital coupling (SOC) was omitted, since SOC mainly affects the localized 4d states, whereas the LSPR arises from the delocalized 5s electrons and is therefore only weakly impacted. Moreover, this effect is already known to have a negligible influence even for smaller Ag clusters.[63]

Author contributions

I. S. conceived the project, prepared figures, performed computational simulations with the SC potential, and conducted data analysis. Z. K. supervised the project, contributed to refining the VDT concept, and developed and updated the Cluster program for SC-based computational simulations. R. F. performed computational simulations with the Gupta potential, conducted data analysis, and contributed to refining the VDT concept. M. C. and H.-C. W. performed TDDFT+*U* computational calculations, performed data analysis, and prepared figures. P. K. contributed to the description of electrochemical properties. All authors contributed to writing the manuscript, discussing the results, and providing comments.

Conflicts of interest

There are no conflicts to declare.

Data availability

All data supporting the findings of this study are provided within the article and its supplementary information (SI). Supplementary information is available. See DOI: https://doi.org/10.1039/d5nr04865f.

Acknowledgements

This work was supported by the Polish National Science Centre (NCN), grant numbers 2022/47/B/ST4/02310 and 2018/29/B/ST4/00710, as well as by the Project PINENUT – CUP D53D23002340006 – Grant Assignment Decree No. 957 adopted on 30/06/2023 by the Italian Ministry of University and Research (MUR).

We acknowledge support from the French National Research Agency (Agence Nationale de Recherche, ANR) in the frame of the project "SchNAPSS", ANR-21-CE09-0021. The work has used HPC and storage resources by GENCI at CINES and IDRIS [grant 2024-0906829] on the supercomputers Jean Zay [CSL] and Adastra [GENOA]. Moreover, the authors acknowledge the contribution of the International Research Network IRN Nanoalloys (CNRS). Mohit C. thanks ED352 of Aix-Marseille University for the PhD scholarship.

References

1 X. Liu, J. Luo and J. Zhu, *Nano Lett.*, 2006, **6**, 408–412.
2 G. Park, K. S. Min, H. Kwon, S. Yoon, S. Park, J. Kwon, S. Lee, J. Jo, M. Kim and S. K. Kim, *Adv. Mater.*, 2021, **33**, 2100653.
3 X. Qian and H. S. Park, *J. Mech. Phys. Solids*, 2010, **58**, 330–345.
4 X. Ma, H. Sun, Y. Wang, X. Wu and J. Zhang, *Nano Energy*, 2018, **53**, 932–939.
5 K. Liu, H. Yang, Y. Jiang, Z. Liu, S. Zhang, Z. Zhang, Z. Qiao, Y. Lu, T. Cheng, O. Terasaki, Q. Zhang and C. Gao, *Nat. Commun.*, 2023, **14**, 2424.
6 D. Kim, M. Chung, J. Carnis, S. Kim, K. Yun, J. Kang, W. Cha, M. J. Cherukara, E. Maxey, R. Harder, K. Sasikumar, S. K. R. S. Sankaranarayanan, A. Zozulya, M. Sprung, D. Riu and H. Kim, *Nat. Commun.*, 2018, **9**, 3422.
7 M. Dupraz, N. Li, J. Carnis, L. Wu, S. Labat, C. Chatelier, R. van de Poll, J. P. Hofmann, E. Almog, S. J. Leake, Y. Watier, S. Lazarev, F. Westermeier, M. Sprung, E. J. M. Hensen, O. Thomas, E. Rabkin and M.-I. Richard, *Nat. Commun.*, 2022, **13**, 3003.
8 T. Nilsson Pingel, M. Jørgensen, A. B. Yankovich, H. Grönbeck and E. Olsson, *Nat. Commun.*, 2018, **9**, 2722.
9 J. Carnis, A. R. Kshirsagar, L. Wu, M. Dupraz, S. Labat, M. Texier, L. Favre, L. Gao, F. E. Oropeza, N. Gazit, E. Almog, A. Campos, J.-S. Micha, E. J. M. Hensen, S. J. Leake, T. U. Schülli, E. Rabkin, O. Thomas, R. Poloni and J. P. Hofmann, *Nat. Commun.*, 2021, **12**, 5303.
10 J. M. Yuk, J. Park, P. Ercius, K. Kim, D. J. Hellebusch, M. F. Crommie, J. Y. Lee, A. Zettl and A. P. Alivisatos, *Science*, 2012, **336**, 61–64.
11 J. M. Yuk, M. Jeong, S. Y. Kim, H. K. Seo, J. Kim and J. Y. Lee, *Chem. Commun.*, 2013, **49**, 11479–11482.
12 E. Y. El Koraychy, C. Roncaglia, D. Nelli, M. Cerbelaud and R. Ferrando, *Nanoscale Horiz.*, 2022, **7**, 883–889.
13 X. Ma, F. Lin, X. Chen and C. Jin, *ACS Nano*, 2020, **14**, 9594–9604.
14 Y. Xia, D. Nelli, R. Ferrando, J. Yuan and Z. Y. Li, *Nat. Commun.*, 2021, **12**, 2905.
15 X. Huang, S. Li, Y. Huang, S. Wu, X. Zhou, S. Li, C. L. Gan, F. Boey, C. A. Mirkin and H. Zhang, *Nat. Commun.*, 2011, **2**, 292.
16 Z. Fan, M. Bosman, Z. Huang, Y. Chen, C. Ling, L. Wu, Y. A. Akimov, R. Laskowski, B. Chen, P. Ercius, J. Zhang, X. Qi, M. H. Goh, Y. Ge, Z. Zhang, W. Niu, J. Wang, H. Zheng and H. Zhang, *Nat. Commun.*, 2020, **11**, 3294.
17 X. Huang, S. Li, S. Wu, Y. Huang, F. Yin, C. L. Gan and H. Zhang, *Adv. Mater.*, 2012, **24**, 979–983.
18 Z. Fan, M. Bosman, X. Huang, D. Huang, Y. Yu, K. P. Ong, Y. A. Akimov, L. Wu, B. Li, J. Wu, Y. Huang, Q. Liu, C. E. Png, C. L. Gan, P. Yang and H. Zhang, *Nat. Commun.*, 2015, **6**, 7684.
19 R. Ferrando, G. Rossi, F. Nita, G. Barcaro and A. Fortunelli, *ACS Nano*, 2008, **2**, 1849–1856.
20 H. Duan, N. Yan, R. Yu, C.-R. Chang, G. Zhou, H.-S. Hu, H. Rong, Z. Niu, J. Mao, H. Asakura, T. Tanaka, P. J. Dyson, J. Li and Y. Li, *Nat. Commun.*, 2014, **5**, 3093.
21 I. Chakraborty, S. N. Shirodkar, S. Gohil, U. V. Waghmare and P. Ayyub, *J. Phys.: Condens. Matter*, 2013, **26**, 025402.
22 V. Tzitzios, G. Basina, M. Gjoka, V. Alexandrakis, V. Georgakilas, D. Niarchos, N. Boukos and D. Petridis, *Nanotechnology*, 2006, **17**, 3750–3755.

23 J. Zhuang, X. Liu, Y. Ji, F. Gu, J. Xu, Y. Han, G. Xu, Z. Zhong and F. Su, *J. Mater. Chem. A*, 2020, **8**, 22143–22154.

24 B. E. Warren, *X-ray Diffraction*, Addison-Wesley, Reading, MA, 1969.

25 R. S. Wagner, *Acta Metall.*, 1960, **8**, 57–60.

26 D. R. Hamilton and R. G. Seidensticker, *J. Appl. Phys.*, 1960, **31**, 1165–1168.

27 B. W. van de Waal, *J. Cryst. Growth*, 1996, **158**, 153–165.

28 G. A. Narvaez, J. Kim and J. W. Wilkins, *Phys. Rev. B: Condens. Matter Mater. Phys.*, 2005, **72**, 155411.

29 H. Portales, N. Goubet, L. Saviot, S. Adichtchev, D. B. Murray, A. Mermet, E. Duval and M.-P. Pileni, *Proc. Natl. Acad. Sci. U. S. A.*, 2008, **105**, 14784–14789.

30 W. Shao, Q. Pan, Q. Chen, C. Zhu, W. Tao, H. Zhu, H. Song, X. Liu, P. Tan, G. Sheng, T. Sun, X. Li and Y. Zhu, *Adv. Funct. Mater.*, 2021, **31**, 2006738.

31 H. Portalès, N. Goubet, L. Saviot, P. Yang, S. Sirotkin, E. Duval, A. Mermet and M.-P. Pileni, *ACS Nano*, 2010, **4**, 3489–3497.

32 Y. Wan, H. Portalès, N. Goubet, A. Mermet and M.-P. Pileni, *Nano Res.*, 2013, **6**, 611–618.

33 Y. Tang and M. Ouyang, *Nat. Mater.*, 2007, **6**, 754–759.

34 S. Link and M. A. El-Sayed, *J. Phys. Chem. B*, 1999, **103**, 8410–8426.

35 N. Tancogne-Dejean, M. J. T. Oliveira and Á. Rubio, *Phys. Rev. B*, 2017, **96**, 245133.

36 M. Chaudhary and H.-C. Weissker, *Nat. Commun.*, 2024, **15**, 9225.

37 M. Chaudhary, J. Lermé and H.-C. Weissker, *Nanoscale*, 2026, DOI: 10.1039/d5nr04178c.

38 I. Smirnov, Z. Kaszkur and A. Hoell, *Nanoscale*, 2023, **15**, 8633–8642.

39 A. Stukowski, *Modell. Simul. Mater. Sci. Eng.*, 2010, **18**, 015012.

40 B. Mierzwa and Z. Kaszkur, in *Applied Crystallography*, World Scientific, 2004, pp. 162–166. DOI: 10.1142/9789812702913_0031.

41 Z. Kaszkur, Cluster – Zbigniew Kaszkur website, available at: https://kaszkur.net.pl/index.php/cluster/ (accessed 27 March 2025).

42 T. Górecki, *Z. Metallkd.*, 1974, **65**, 426–431.

43 Q. S. Mei and K. Lu, *Prog. Mater. Sci.*, 2007, **52**, 1175–1262.

44 G. Kresse and J. Furthmüller, *Comput. Mater. Sci.*, 1996, **6**, 15–50.

45 G. Kresse and D. Joubert, *Phys. Rev. B:Condens. Matter Mater. Phys.*, 1999, **59**, 1758–1775.

46 T. Tsukamoto, N. Haruta, T. Kambe, A. Kuzume and K. Yamamoto, *Nat. Commun.*, 2019, **10**, 4519.

47 W. Li, D. Wang, Y. Zhang, L. Tao, T. Wang, Y. Zou, Y. Wang, R. Chen and S. Wang, *Adv. Mater.*, 2020, **32**, 1907879.

48 Y. Li, Y. Sun, Y. Qin, W. Zhang, L. Wang, M. Luo, H. Yang and S. Guo, *Adv. Energy Mater.*, 2020, **10**, 1903120.

49 P. Strasser, S. Koh, T. Anniyev, J. Greeley, K. More, C. Yu, Z. Liu, S. Kaya, D. Nordlund, H. Ogasawara, M. F. Toney and A. Nilsson, *Nat. Chem.*, 2010, **2**, 454–460.

50 I. E. L. Stephens, A. S. Bondarenko, F. J. Perez-Alonso, F. Calle-Vallejo, L. Bech, T. P. Johansson, A. K. Jepsen, R. Frydendal, B. P. Knudsen, J. Rossmeisl and I. Chorkendorff, *J. Am. Chem. Soc.*, 2011, **133**, 5485–5491.

51 W. Zhong, Y. Liu and D. Zhang, *J. Phys. Chem. C*, 2012, **116**, 2994–3000.

52 C. Wang, Y. Shi, D.-R. Yang and X.-H. Xia, *Curr. Opin. Electrochem.*, 2018, **7**, 95–102.

53 C. H. Choi, K. Chung, T.-T. H. Nguyen and D. H. Kim, *ACS Energy Lett.*, 2018, **3**, 1415–1433.

54 Y. Wang, T. Wang, H. Arandiyan, G. Song, H. Sun, Y. Sabri, C. Zhao, Z. Shao and S. Kawi, *Adv. Mater.*, 2024, **36**, 2313378.

55 I. Smirnov, *Morphology evolution in mono- and bimetallic fcc nanoparticles*, PhD thesis, Institute of Physical Chemistry, Warsaw, 2023; available at RCIN (accessed 27 March 2025).

56 A. P. Sutton and J. Chen, *Philos. Mag. Lett.*, 1990, **61**, 139–146.

57 C. Zhu, R. H. Byrd, P. Lu and J. Nocedal, *ACM Trans. Math. Softw.*, 1997, **23**, 550–560.

58 I. Breßler, J. Kohlbrecher and A. F. Thünemann, *J. Appl. Crystallogr.*, 2015, **48**, 1587–1598.

59 J. P. Perdew, K. Burke and M. Ernzerhof, *Phys. Rev. Lett.*, 1996, **77**, 3865–3868.

60 N. Tancogne-Dejean, T. Oliveira, X. Andrade, H. Appel, C. H. Borca, G. Le Breton, F. Buchholz, A. Castro, S. Corni, A. A. Correa, U. De Giovannini, A. Delgado, F. G. Eich, J. Flick, G. Gil, A. Gómez, N. Helbig, H. Hübener, R. Jestädt, J. Jornet-Somoza, *et al.*, *J. Chem. Phys.*, 2020, **152**, 124119.

61 N. Troullier and J. L. Martins, *Phys. Rev. B:Condens. Matter Mater. Phys.*, 1991, **43**, 1993–2006.

62 K. Yabana and G. F. Bertsch, *Phys. Rev. B:Condens. Matter Mater. Phys.*, 1996, **54**, 4484–4487.

63 N. Ghazi, M. S. Islam and T. Ahmed, *RSC Adv.*, 2014, **4**, 13001–13011.